CrossMark

PEER REVIEWED

Air Plasma-Sprayed La$_2$Zr$_2$O$_7$-SrZrO$_3$ Composite Thermal Barrier Coating Subjected to CaO-MgO-Al$_2$O$_3$-SiO$_2$ (CMAS)

Lili Cai[1,2] · Wen Ma[1,2] · Bole Ma[1,2] · Feng Guo[1,2] · Weidong Chen[1,2] · Hongying Dong[2,3] · Yingchai Shuang[2,3]

Abstract La$_2$Zr$_2$O$_7$-SrZrO$_3$ composite thermal barrier coatings (TBCs) were prepared by air plasma spray (APS). The La$_2$Zr$_2$O$_7$-SrZrO$_3$ composite TBCs covered with calcium-magnesium-aluminum-silicate (CMAS) powder, as well as the powder mixture of CMAS and spray-dried La$_2$Zr$_2$O$_7$-SrZrO$_3$ composite powder, were heat-treated at 1250 °C in air for 1, 4, 8, and 12 h. The phase constituents and microstructures of the reaction products were characterized by x-ray diffraction, scanning electron microscopy, and energy-dispersive spectroscopy. Experimental results showed that the La$_2$Zr$_2$O$_7$-SrZrO$_3$ composite TBCs had higher CMAS resistance than 8YSZ coating. A dense new layer developed between CMAS and La$_2$Zr$_2$O$_7$-SrZrO$_3$ composite TBCs during interaction, and this new layer consisted mostly of apatite (Ca$_2$La$_8$(SiO$_4$)$_6$O$_2$) and c-ZrO$_2$. The newly developed layer effectively protected the La$_2$Zr$_2$O$_7$-SrZrO$_3$ composite TBCs from further CMAS attack.

Keywords apatite · CMAS · La$_2$Zr$_2$O$_7$ · SrZrO$_3$ · thermal barrier coatings

Introduction

Thermal barrier coatings (TBCs) with low thermal conductivity, high thermal expansion coefficient (TEC), and acceptable phase stability were applied widely in aero engine turbine blades, thus reducing surface temperature while enhancing engine efficiency (Ref 1). State-of-the-art TBCs are based on 7-8 wt.% Y$_2$O$_3$-stabilized ZrO$_2$ (8YSZ). However, the maximum operation temperature of 8YSZ is limited to 1200 °C for long-term applications. At high temperatures, the phase transitions, accelerated sintering effect, and degradation caused by calcium-magnesium-aluminum-silicate (CMAS) melts result in the premature failure of the 8YSZ TBCs (Ref 2-5). The development of new TBC candidates, which provide high inlet temperatures while increasing engine efficiency and reducing emission, is investigated to satisfy the demands of the next-generation advanced turbine engines.

Among the newly developed TBC candidates, La$_2$Zr$_2$O$_7$ with the pyrochlore structure has low thermal conductivity and acceptable phase stability. However, its fracture toughness and TEC are relatively low (Ref 6, 7). Another TBC candidate material, SrZrO$_3$ with the perovskite structure, has high melting point (2650 °C) and TEC (10.9 × 10^{-6}K^{-1}) and also exhibits excellent thermal cycling performance above 1250 °C (Ref 8, 9). However, SrZrO$_3$ undergoes three phase transitions from room temperature to high temperature, and the transformation from orthorhombic *Pnma* to pseudo-tetragonal *Imma* at 700 °C involves a volume change of ∼0.14% (Ref 10).

Ceramic composites can effectively overcome the inherent brittleness and inferior mechanical properties of this single-phase ceramic material. La$_2$Zr$_2$O$_7$-La$_2$Ce$_2$O$_7$ composite has better anti-sintering properties and lower thermal conductivity compared with La$_2$Zr$_2$O$_7$ and

✉ Wen Ma
wma66@163.com; wma@imut.edu.cn

1   School of Materials Science and Engineering, Inner Mongolia University of Technology, Hohhot 010051, China

2   Inner Mongolia Key Laboratory of Thin Film and Coatings Technology, Inner Mongolia University of Technology, Hohhot 010051, China

3   School of Chemical Engineering, Inner Mongolia University of Technology, Hohhot 010051, China

$La_2Ce_2O_7$ (Ref [11]). The Al_2O_3-YSZ composite coating exhibits better thermal insulation effect and superior thermal shock resistance compared with YSZ coating (Ref [12]). The spark plasma-sintered (SPS) $La_2Zr_2O_7$-$SrZrO_3$ composite inhibits $SrZrO_3$ from phase transitions effectively. The fracture toughness (1.95 ± 0.06 MPa m$^{1/2}$) and the thermal conductivity (0.91 W m^{-1} K^{-1}) of $La_2Zr_2O_7$-$SrZrO_3$ composite are superior to $La_2Zr_2O_7$ and $SrZrO_3$. Therefore, $La_2Zr_2O_7$-$SrZrO_3$ composite becomes a promising TBC candidate material (Ref [13]).

With the increased surface temperature of TBCs that exceeded the melting temperatures of CMAS (melting temperatures: 1150-1250 °C), the degradation of TBC subjected to CMAS melts has become a crucial issue in the development of next-generation gas turbine engines. In recent years, the interaction of some new TBC candidate materials subjected to CMAS is investigated (Ref [14-16]). The pyrochlore TBCs, such as $Gd_2Zr_2O_7$ and $La_2Zr_2O_7$, have attracted much attention due to their promising resistance against CMAS attack (Ref [14], [17]). They rapidly dissolve into the CMAS melt, and a crystalline apatite is precipitated concurrently, which arrests the penetration of the molten CMAS front.

In this study, the microstructure evolution of the $La_2Zr_2O_7$-$SrZrO_3$ composite coating under CMAS attack at 1250 °C for different times was investigated. The interaction mechanism of the coating under CMAS attack was also explored.

Experimental Procedure

In the present study, the $La_2Zr_2O_7$-$SrZrO_3$ composite powder was synthesized by solid-state reaction at 1450 °C for 12 h using La_2O_3 (99.99%, Grirem Advanced Materials Co., Ltd., China), ZrO_2 (99.99%, Grirem Advanced Materials Co., Ltd., China), and $SrCO_3$ (>98%, Shanghai Reagent Co., Ltd., China) as the starting materials.

For plasma spraying, the synthesized $La_2Zr_2O_7$-$SrZrO_3$ composite powder was milled with deionized water and subsequently spray-dried. Sieved-size fractions between 45 and 100 μm were used for plasma spraying. The $La_2Zr_2O_7$-$SrZrO_3$ composite coatings were plasma-sprayed (Model MC 60, Medicoat AG, Mägenwil, Switzerland) on IN718 superalloy substrates with a diameter of 30 mm and a thickness of 3 mm. The spray parameters for the coatings are listed in Table 1. Before depositing the $La_2Zr_2O_7$-$SrZrO_3$ composite coating, the substrate surface was roughened by grit blasting using Al_2O_3 #24 grit, followed by ultrasonic cleaning using ethanol and acetone successively.

The selected CMAS model had a chemical composition of 33CaO-9MgO-13AlO$_{1.5}$-45SiO$_2$ (mol.%) (Ref [5], [14], [18], [19]) using CaO, MgO, Al_2O_3, and SiO_2 powders (AR, Grecia Chemical Technology Co., Ltd., China) as the starting materials. The CMAS was prepared by mixing these oxides and milling them in deionized water to form a thick paste, which was subsequently applied to the surface of the TBC specimens with a concentration of 30 mg/cm^2. After drying, the specimens were heat-treated at 1250 °C for 1, 4, 8, and 12 h. To better understand the phase constituents of the reaction products, the CMAS powder was mixed with the $La_2Zr_2O_7$-$SrZrO_3$ composite powder with a weight ratio of 1:1 by ball milling, followed by heat treatment under the same conditions as the TBC specimens.

The phase constituents of the $La_2Zr_2O_7$-$SrZrO_3$ composite powder and coating, as well as the mixture of the CMAS powder and the $La_2Zr_2O_7$-$SrZrO_3$ composite powder after heat treatment at 1250 °C, were identified by x-ray diffraction (XRD; model D/MAX 2200, Rigaku Co., Ltd., Japan). A scanning electron microscopy (SEM; model JXA 840, JEOL, Japan) equipped with energy-dispersive spectroscopy (EDS) was used for microstructure analyses. All samples for cross-sectional analysis were initially embedded in transparent epoxy resin and then polished with diamond pastes down to 1 μm.
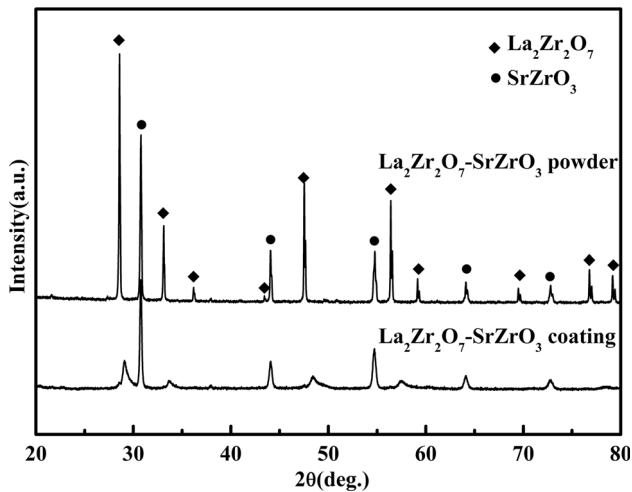
Results

Phase Analyses of the $La_2Zr_2O_7$-$SrZrO_3$ Composite Powder and Its Coating

The XRD patterns of the synthesized $La_2Zr_2O_7$-$SrZrO_3$ composite powder and its as-sprayed coating are shown in Fig. 1. The synthesized $La_2Zr_2O_7$-$SrZrO_3$ composite powder consisted $La_2Zr_2O_7$ with the pyrochlore structure and $SrZrO_3$ with the perovskite structure. Both phases crystallized appropriately, and no other impurity phase was observed. For the APS-sprayed $La_2Zr_2O_7$-$SrZrO_3$ composite coating, the diffraction peaks were broadened, and the peak intensities decreased for $La_2Zr_2O_7$ and $SrZrO_3$, especially for $La_2Zr_2O_7$. The reasons for these results are as follows. The molten droplets during plasma spraying reach the substrate and solidify to form a coating in an extremely short time, resulting in the development of

Table 1 Spray parameters of the $La_2Zr_2O_7$-$SrZrO_3$ coating

Gun current, A	Spray distance, mm	Hydrogen flow rate, L/min	Argon flow rate, L/min
550	110	12	35

metastable phase or an inappropriate crystallized phase. In addition, the composite coating may have high activation energy for grain growth of $La_2Zr_2O_7$ and $SrZrO_3$. The $La_2Zr_2O_7$-YSZ nano-composite powder has much higher activation energy for grain growth of $La_2Zr_2O_7$ and YSZ than its single-phase counterparts (Ref 20).

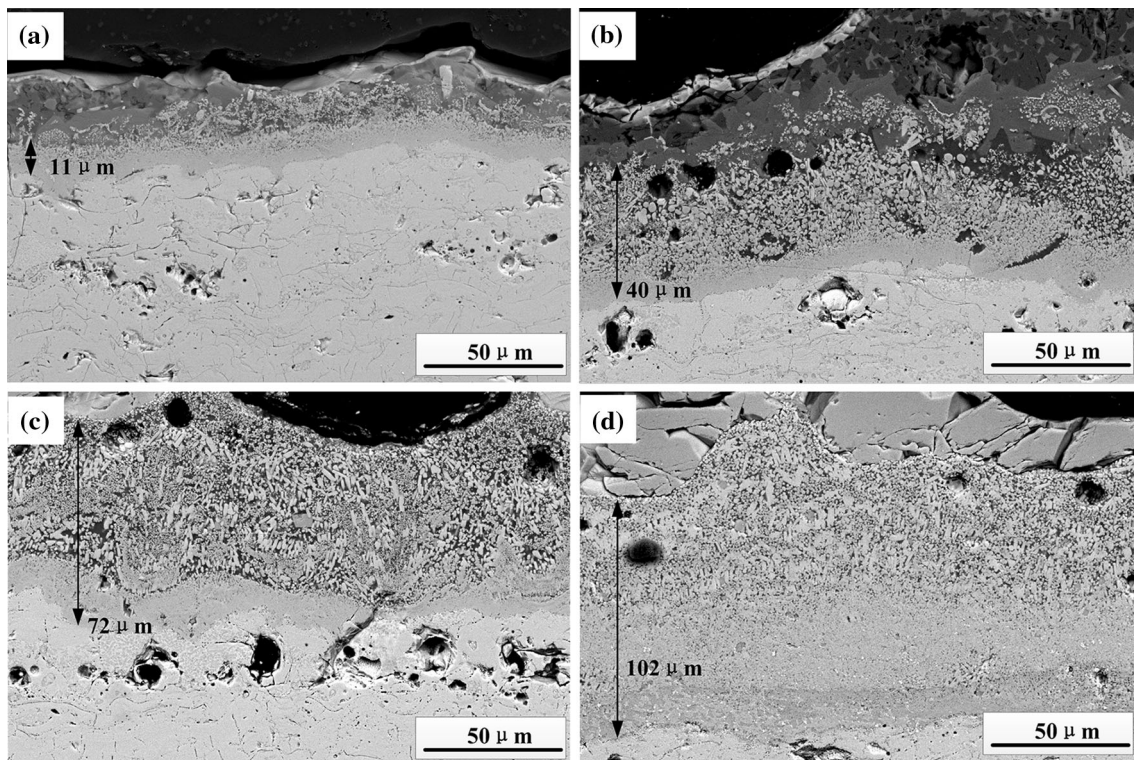**Fig. 1** XRD patterns of the $La_2Zr_2O_7$-$SrZrO_3$ composite powder and its as-sprayed coating

Interaction Behavior Between the $La_2Zr_2O_7$-$SrZrO_3$ Composite Coating and the Molten CMAS

Figure 2 shows the cross-sectional microstructures of the $La_2Zr_2O_7$-$SrZrO_3$ composite coatings after CMAS attack at 1250 °C for different times. The interaction layer thickness of the composite coating increases gradually to approximately 11, 40, 72, and 102 μm as the interaction time increases after CMAS attack at 1250 °C for 1, 4, 8, and 12 h, respectively. On the contrary, the thickness of the interaction layer of the 8YSZ coating was approximately 250 μm within 12 h heat treatment at 1250 °C (Ref 15), indicating that the $La_2Zr_2O_7$-$SrZrO_3$ composite coatings have superior CMAS resistance than the 8YSZ coating. The interaction layer of the $La_2Zr_2O_7$-$SrZrO_3$ composite coatings comprised the inner dense layer and outer porous layer. The rod-shaped particles and globular particles have developed clearly in the porous layer after CMAS attack for 4 h as shown in Fig. 2(b).

The high-magnification cross-sectional microstructures of the $La_2Zr_2O_7$-$SrZrO_3$ composite coating after CMAS attack at 1250 °C for 1 h are shown in Fig. 3. Evidently, rod-shaped particles and globular particles have formed in the interaction layer. In addition, some globular particles disperse in the CMAS melt. Above the interaction layer, the two distinct phases are marked as "1" (dark gray

Fig. 2 Cross-sectional microstructures of the $La_2Zr_2O_7$-$SrZrO_3$ composite coatings after CMAS attack at 1250 °C for: (a) 1 h, (b) 4 h, (c) 8 h, (d) 12 h
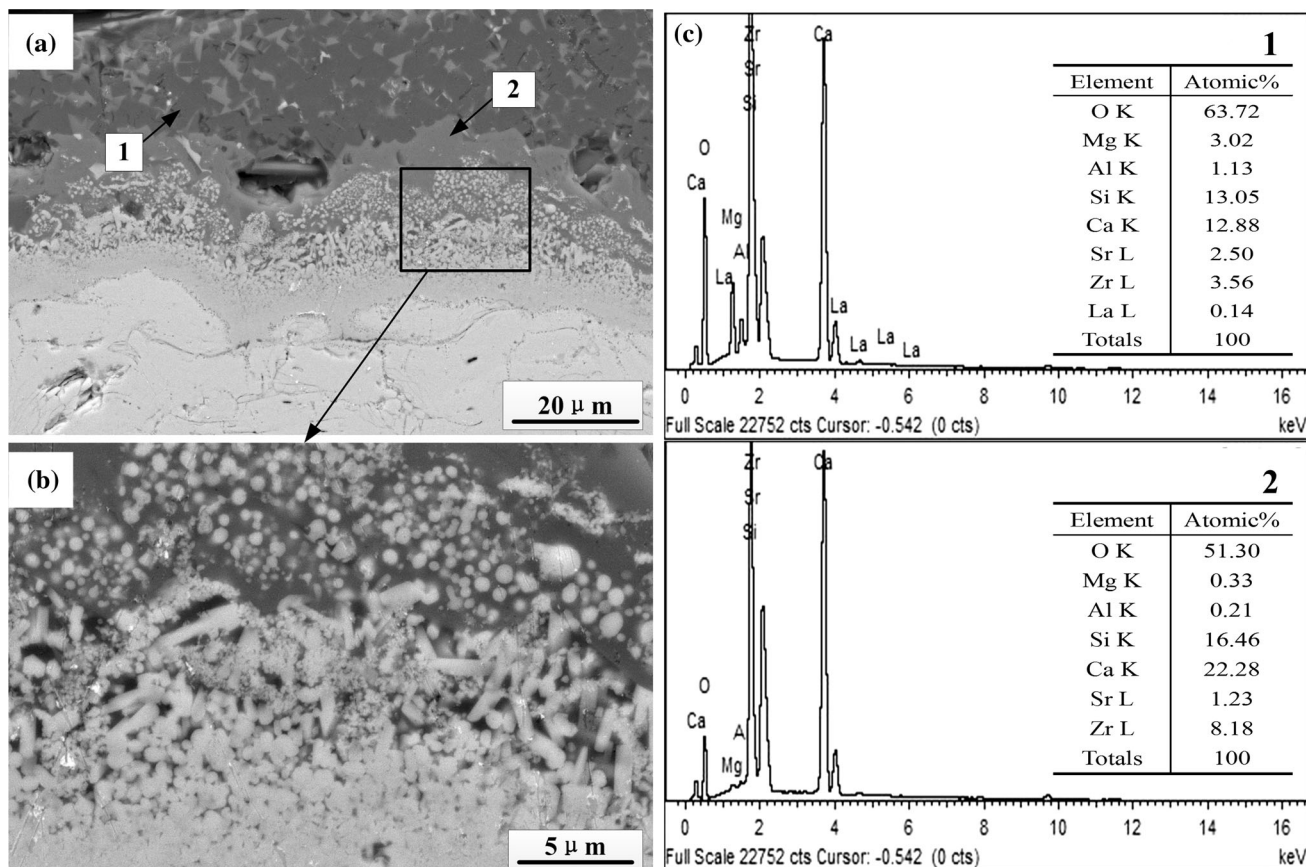
phase) and "2" (light gray phase), as shown in Fig. 3(a), and the EDS analyses of the two phases are shown in Fig. 3(c). The dark gray phase is mainly composed of Ca, Si, Zr, Mg, and Sr with traces of Al and La, indicating that the formation of the dark gray phase results from a chemical interaction between the CMAS and the $La_2Zr_2O_7$-$SrZrO_3$ composite coating. The light gray phase is mainly composed of Ca, Si, and Zr with traces of Sr, Mg, and Al.

Some CMAS remain on the $La_2Zr_2O_7$-$SrZrO_3$ composite coating surface after CMAS attack at 1250 °C, resulting in the difficulty to identify the reaction products by XRD. Therefore, to identify the reaction products between the CMAS and the $La_2Zr_2O_7$-$SrZrO_3$ composite coating, a mixture of the CMAS powder and the $La_2Zr_2O_7$-$SrZrO_3$ composite powder (weight ratio: 1:1) was ball-milled homogeneously and then heat-treated at 1250 °C for different times. The XRD patterns of the heat-treated powder mixture are shown in Fig. 4. Apart from the $La_2Zr_2O_7$ and $SrZrO_3$, La-apatite ($Ca_2La_8(SiO_4)_6O_2$), fluorite (c-ZrO_2), mellilite ($Ca_2MgSi_2O_7$), and baghdadite ($Ca_3ZrSi_2O_9$) were developed as the reaction products. The content of $La_2Zr_2O_7$ decreases as the reaction time increases from 1 to 8 h and then remains almost constant with increasing reaction time, indicating that $La_2Zr_2O_7$ reacts severely with the CMAS powder. However, minor $SrAl_2Si_2O_8$ developed after CMAS attack for different times, indicating much less chemical reaction taking place between CMAS and $SrZrO_3$.

Combined with the EDS and XRD analyses, the dark gray phase "1" and light gray phase "2" in Fig. 3(a) are identified as mellilite ($Ca_2MgSi_2O_7$) and baghdadite ($Ca_3ZrSi_2O_9$) solid solutions with minor other elements. Sr element has been detected both in dark gray phase "1" and light gray phase "2" (Fig. 3c), indicating the disintegration of $SrZrO_3$ during CMAS attack. Sr element may dissolve into $Ca_2MgSi_2O_7$ and $Ca_3ZrSi_2O_9$ due to the similar ion radius between Sr^{2+} (0.113 nm) and Ca^{2+} (0.118 nm).

The reaction products are summarized in Table 2 based on the XRD results of the powder mixture of $La_2Zr_2O_7$-$SrZrO_3$ and CMAS (Fig. 4). Except for the as-sprayed coating compositions of $La_2Zr_2O_7$ and $SrZrO_3$, the major reaction products are fluorite (c-ZrO_2) and La-apatite ($Ca_4La_6(SiO_4)_6O$ or/and $Ca_2La_8(SiO_4)_6O_2$) after CMAS attack for varied times. The $Ca_4La_6(SiO_4)_6O$ transforms into $Ca_2La_8(SiO_4)_6O_2$ after CMAS attack at 1250 °C for 8 h. Additionally, Mg_2SiO_4, $Ca_3ZrSi_2O_9$, and $SrAl_2Si_2O_8$,

Element	Atomic%
O K	63.72
Mg K	3.02
Al K	1.13
Si K	13.05
Ca K	12.88
Sr L	2.50
Zr L	3.56
La L	0.14
Totals	100

Full Scale 22752 cts Cursor: -0.542 (0 cts)

Element	Atomic%
O K	51.30
Mg K	0.33
Al K	0.21
Si K	16.46
Ca K	22.28
Sr L	1.23
Zr L	8.18
Totals	100

Full Scale 22752 cts Cursor: -0.542 (0 cts)

Fig. 3 High-magnification cross-sectional microstructures and EDS analyses of the $La_2Zr_2O_7$-$SrZrO_3$ composite coating after CMAS attack at 1250 °C for 1 h
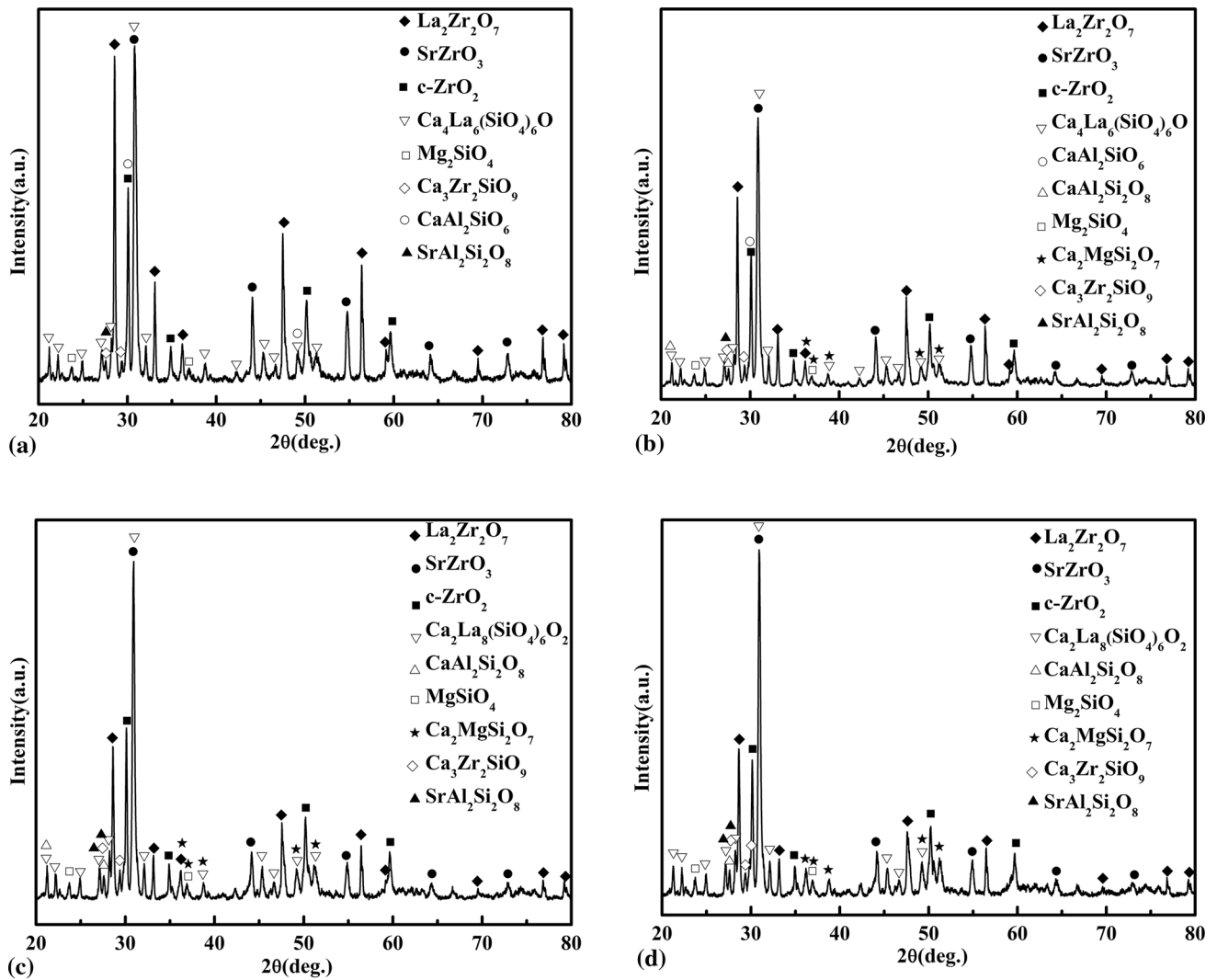
Fig. 4 XRD patterns of the powder mixture of $La_2Zr_2O_7$-$SrZrO_3$ and CMAS after heat treatment at 1250 °C: (a) 1 h, (b) 4 h, (c) 8 h, (d) 12 h

Table 2 Reaction products of the powders mixture of $La_2Zr_2O_7$-$SrZrO_3$ and CMAS

Reaction products	1250 °C			
	1, h	4, h	8, h	12, h
Major products	c-ZrO_2	c-ZrO_2	c-ZrO_2	c-ZrO_2
	$Ca_4La_6(SiO_4)_6O$	$Ca_4La_6(SiO_4)_6O$	$Ca_2La_8(SiO_4)_6O_2$	$Ca_2La_8(SiO_4)_6O_2$
Minor products	$CaAl_2SiO_6$	$CaAl_2SiO_6$	…	…
	…	$CaAl_2Si_2O_8$	$CaAl_2Si_2O_8$	$CaAl_2Si_2O_8$
	Mg_2SiO_4	Mg_2SiO_4	Mg_2SiO_4	Mg_2SiO_4
	…	$Ca_2MgSi_2O_7$	$Ca_2MgSi_2O_7$	$Ca_2MgSi_2O_7$
	$Ca_3ZrSi_2O_9$	$Ca_3ZrSi_2O_9$	$Ca_3ZrSi_2O_9$	$Ca_3ZrSi_2O_9$
	$SrAl_2Si_2O_8$	$SrAl_2Si_2O_8$	$SrAl_2Si_2O_8$	$SrAl_2Si_2O_8$

as minor reaction products, coexist after different interaction times. However, $CaAl_2SiO_6$ develops after CMAS attack for 1 h, and it transforms into $CaAl_2Si_2O_8$ gradually with more SiO_2 incorporated as the interaction time

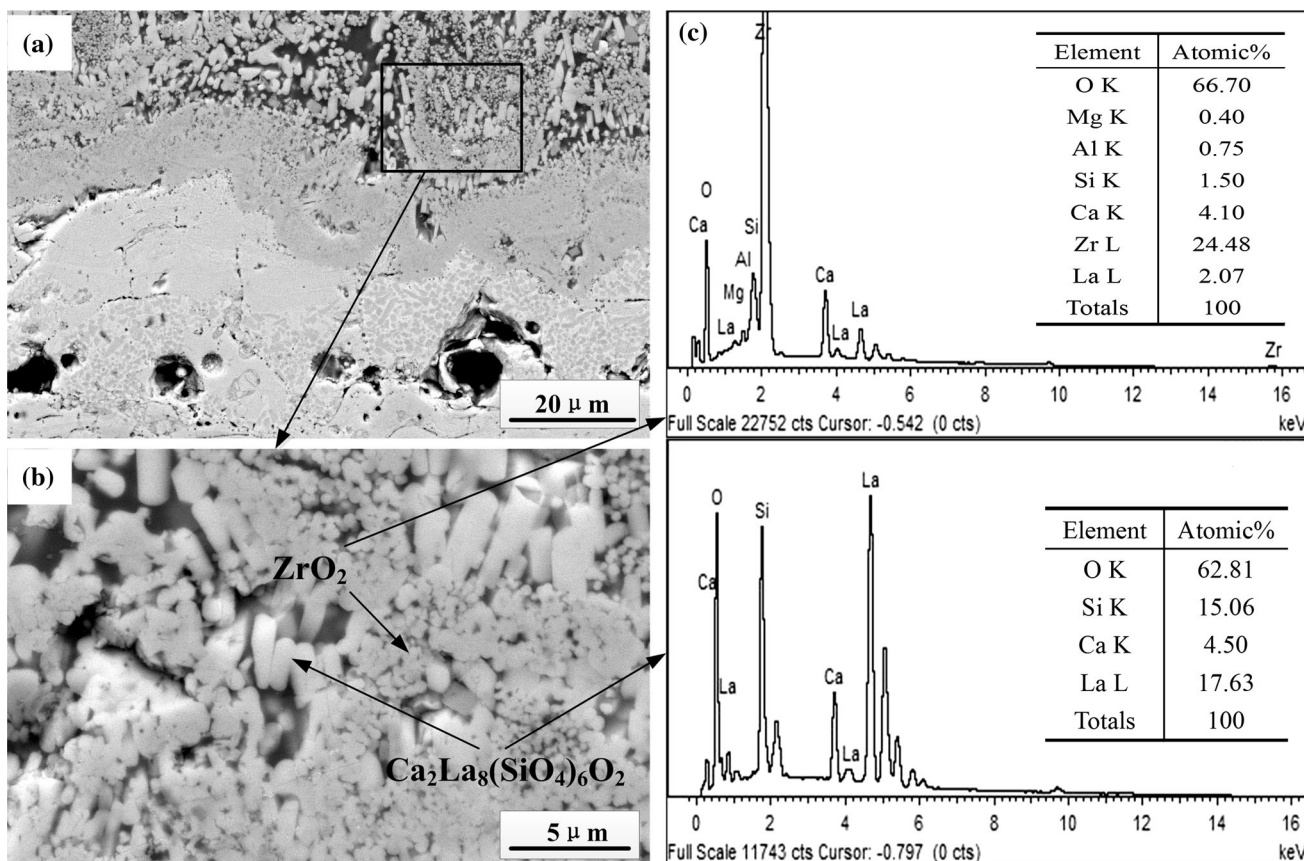increases. $CaAl_2SiO_6$ and $CaAl_2Si_2O_8$ are obtained after 4-h interaction, and only $CaAl_2Si_2O_8$ is found after 8-h interaction. With increasing interaction time, more CaO, MgO, and SiO_2 generate $Ca_2MgSi_2O_7$. The development of

$SrAl_2Si_2O_8$ is due to the disintegration of $SrZrO_3$ and resulted from the chemical reaction of SrO with Al_2O_3 and SiO_2.

The rod-shaped and globular particles in the interaction layer grow gradually as the interaction time increases, which are clearly shown in the high-magnification cross-sectional microstructures of the $La_2Zr_2O_7$-$SrZrO_3$ composite coating after CMAS attack at 1250 °C for 8 h (Fig. 5). The rod-shaped particles comprised Ca, La, and Si by EDS analysis and can be confirmed as La-apatite ($Ca_2La_8(SiO_4)_6O_2$) with XRD analysis. The globular particles consist primarily of Zr with litter amount of Ca, La, Mg, and Al and can be identified as fluorite (c-ZrO_2) based on the XRD result (Fig. 4). The rod-shaped La-apatite particles and globular fluorite particles are interpenetrated by residual CMAS melt. As shown in Fig. 5(a), the size of the crystalline La-apatite decreases toward the interface between the interaction layer and the $La_2Zr_2O_7$-$SrZrO_3$ composite coating, because the crystals closer to the outer surface are likely to have formed earlier and have more time to coarsen. In addition, the relative amount of CMAS decreases toward the interface.

Discussion

The experimental results reveal that the microstructures of the $La_2Zr_2O_7$-$SrZrO_3$ composite coating vary significantly with increasing interaction time at 1250 °C, whereas the reaction products are relatively insensitive to the interaction time. Most of the CMAS/$La_2Zr_2O_7$-$SrZrO_3$ interaction features seem to be in good agreement with the observations in the $La_2Zr_2O_7$ case (Ref 5, 21). The most important reaction product is the La-apatite. The EDS/XRD results indicate that the apatite produced in this study is a silicate phase, which is either in the form of $Ca_4La_6(SiO_4)_6O$ or $Ca_2La_8(SiO_4)_6O_2$ depending on the interaction time. After CMAS attack for 8 h, more La^{3+} react with CMAS; thus, $Ca_4La_6(SiO_4)_6O$ transforms into $Ca_2La_8(SiO_4)_6O_2$ (JCPDS no.29-0337). The general formula of apatite phase is $A_4^I A_6^{II}(SiO_4)_6O_x$, where the "A" sites are occupied by alkali metal, alkaline earth metal, or rare earth ions; x is determined by the net valence of the "A" sites. A^I is occupied by larger radius of Ca^{2+} with ninefold coordination, and A^{II} is occupied by smaller radius with

Element	Atomic%
O K	66.70
Mg K	0.40
Al K	0.75
Si K	1.50
Ca K	4.10
Zr L	24.48
La L	2.07
Totals	100

Full Scale 22752 cts Cursor: -0.542 (0 cts)

Element	Atomic%
O K	62.81
Si K	15.06
Ca K	4.50
La L	17.63
Totals	100

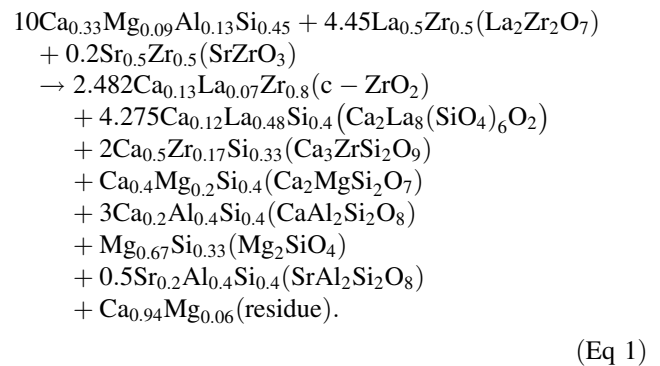Full Scale 11743 cts Cursor: -0.797 (0 cts)

Fig. 5 High-magnification cross-sectional microstructures and EDS analyses of the $La_2Zr_2O_7$-$SrZrO_3$ coatings after CMAS attack at 1250 °C for 8 h

sevenfold coordination relatively (Ref [14], [19]). The initial chemical formula of La-apatite is $Ca_4La_6(SiO_4)_6O$. Some La^{3+} can substitute Ca^{2+} to form $Ca_2La_8(SiO_4)_6$ O_2 because the radius of La^{3+} (0.110 nm) is similar to that of Ca^{2+} (0.118 nm). When more La^{3+} ions react with CMAS, a more stable apatite phase similar to $Gd_2Zr_2O_7$ (Ref [4], [22]) can be produced. After CMAS attack for 12 h, the reaction products are invariant in the mixed powder, and the reaction tends to be stable.

The second reaction product of $La_2Zr_2O_7$-$SrZrO_3$, which is subjected to CMAS, is fluorite c-ZrO_2. EDS determined that the fluorite c-ZrO_2 is stabilized predominantly by CaO and La_2O_3, although less amounts of Mg, Al, and Si are involved.

One possible CMAS interaction mechanism of the $La_2Zr_2O_7$-$SrZrO_3$ coating is dissolution-reprecipitation mechanism (Ref [14], [19]). The CMAS mixture starts to melt at 1250 °C, and $La_2Zr_2O_7$ grains in the $La_2Zr_2O_7$-$SrZrO_3$ coating are wetted by molten CMAS melt and reacted with the melt. The dissolution of the original $La_2Zr_2O_7$-$SrZrO_3$ coating occurs with incorporation and migration of La, Zr, and Sr to the melt. The concentration of La in CMAS melt that accumulates to a certain value triggers the crystallization of La-rich melt into La-apatite. In addition, fluorite crystallizes when the Zr content in the melt exceeds the threshold for nucleation. At the same time, mellilite (Ca_2 $MgSi_2O_7$) and baghdadite ($Ca_3ZrSi_2O_9$) solid solutions with minor other elements in the melt are formed. However, $SrZrO_3$ in the $La_2Zr_2O_7$-$SrZrO_3$ coating reacts much less intensively with CMAS compared to $La_2Zr_2O_7$. In our study, identifying $SrZrO_3$ in the interaction layer is difficult, whereas minor amount of Sr is detected in mellilite and baghdadite. The interaction behavior of $SrZrO_3$ in the $La_2Zr_2O_7$-$SrZrO_3$ coating in contact with CMAS melt at high temperatures requires further investigations in the future.

The interaction behavior of the $La_2Zr_2O_7$-$SrZrO_3$ coating in contact with CMAS melt is extremely similar to $La_2Zr_2O_7$. The Poerschke's results (Ref [19]) and our experimental results indicated that only the dissolution of the $La_2Zr_2O_7$-$SrZrO_3$ coating in the CMAS melt and reprecipitation of apatite and fluorite are sufficiently fast compared to the CMAS penetration through the coating; the CMAS mitigation goal of the coating can be realized. According to the SEM/EDS results, the dense interaction layer mainly comprised La-apatite and globular fluorite (c-ZrO_2) grains that can effectively protect the coating from CMAS penetration. The reaction between the $La_2Zr_2O_7$-$SrZrO_3$ coating and the CMAS melt can occur at high temperature as follows, and the ratio of Ca to La in $Ca_2La_8(SiO_4)_6O_2$ is calculated according to Fig. 5(c).

$$\begin{aligned}
&10Ca_{0.33}Mg_{0.09}Al_{0.13}Si_{0.45} + 4.45La_{0.5}Zr_{0.5}(La_2Zr_2O_7) \\
&\quad + 0.2Sr_{0.5}Zr_{0.5}(SrZrO_3) \\
&\rightarrow 2.482Ca_{0.13}La_{0.07}Zr_{0.8}(c-ZrO_2) \\
&\quad + 4.275Ca_{0.12}La_{0.48}Si_{0.4}(Ca_2La_8(SiO_4)_6O_2) \\
&\quad + 2Ca_{0.5}Zr_{0.17}Si_{0.33}(Ca_3ZrSi_2O_9) \\
&\quad + Ca_{0.4}Mg_{0.2}Si_{0.4}(Ca_2MgSi_2O_7) \\
&\quad + 3Ca_{0.2}Al_{0.4}Si_{0.4}(CaAl_2Si_2O_8) \\
&\quad + Mg_{0.67}Si_{0.33}(Mg_2SiO_4) \\
&\quad + 0.5Sr_{0.2}Al_{0.4}Si_{0.4}(SrAl_2Si_2O_8) \\
&\quad + Ca_{0.94}Mg_{0.06}(residue).
\end{aligned}$$

(Eq 1)

The residue is used to balance the equation.

Conclusions

$La_2Zr_2O_7$-$SrZrO_3$ coatings prepared by APS were exposed to CMAS melts at 1250 °C and characterized in terms of microstructure and phase evolution. During CMAS attack, the microstructures of coatings significantly varied with prolonged interaction time, but the reaction products were relatively unaffected. The $La_2Zr_2O_7$-$SrZrO_3$ coating rapidly dissolved in molten CMAS, and La-apatite (Ca_2 $La_8(SiO_4)_6O_2$) and fluorite c-ZrO_2 stabilized mainly with Ca and La precipitating concurrently. The acceptable CMAS resistance for the $La_2Zr_2O_7$-$SrZrO_3$ coating relative to 8YSZ coating in terms of infiltration depth was due to the formation of a dense interaction layer resulting from the fast chemical reactions between $La_2Zr_2O_7$ and CMAS. The interaction mechanism of $La_2Zr_2O_7$-$SrZrO_3$ coating subjected to CMAS was dissolution-reprecipitation, which was similar to that of $La_2Zr_2O_7$.

References

1. N.P. Padture, M. Gell, and E.H. Jordan, Thermal Barrier Coatings for Gas-Turbine Engine Applications, *Science*, 2002, **296**(5566), p 280-284 (in English)

2. D.R. Clarke and S.R. Philpot, Thermal Barrier Coating Materials, *Mater. Today*, 2005, **8**(6), p 22-29 (in English)

3. J.A. Krogstad, R.M. Leckie, S. Krämer, J.M. Cairney, D.M. Liplin, C.A. Jhonson, and C.G. Levi, Phase Evolution Upon Aging of Air Plasma Sprayed *t*'-Zirconia Coatings: I-Microstructure Evolution, *J. Am. Ceram. Soc.*, 2013, **96**(1), p 299-307 (in English)

4. A.D. Gledhill, K.M. Reddy, J.M. Drexler, K. Shinoda, S. Sampath, and N.P. Padture, Mitigation of Damage from Molten Fly Ash to Air-Plasma-Sprayed Thermal Barrier Coatings, *Mater. Sci. Eng., A*, 2011, **528**(24), p 7214-7221 (in English)

5. S. Krämer, J. Yang, and C.G. Levi, Thermochemical Interaction of Thermal Barrier Coatings with Molten CaO–MgO–Al$_2$O$_3$–SiO$_2$ (CMAS) Deposits, *J. Am. Ceram. Soc.*, 2006, **89**(10), p 3167-3175 (in English)

6. X.Q. Cao, R. Vassen, and D. Stoever, Ceramic Materials for Thermal Barrier Coatings, *J. Eur. Ceram. Soc.*, 2004, **24**(1), p 1-10 (in English)

7. K. Jiang, S.B. Liu, G.H. Ma, and L.L. Zhao, Microstructure and Mechanical Properties of La$_2$Zr$_2$O$_7$–(Zr$_{0.92}$Y$_{0.08}$)O$_{1.96}$ Composite Ceramics Prepared by Spark Plasma Sintering, *Ceram. Int.*, 2014, **40**(9), p 13979-13985 (in English)

8. R. Vassen, X.Q. Cao, F. Tietz, D. Basu, and D. Stöver, Zirconates as New Materials for Thermal Barrier Coatings, *J. Am. Ceram. Soc.*, 2000, **83**(8), p 2023-2028 (in English)

9. W. Ma, D. Mack, J. Malzbender, R. Vaßen, and D. Stöver, Yb$_2$O$_3$ and Gd$_2$O$_3$ Doped Strontium Zirconate for Thermal Barrier Coatings, *J. Eur. Ceram. Soc.*, 2008, **28**(16), p 3071-3081 (in English)

10. Y.S. Zhao and D.J. Weidner, Thermal Expansion of SrZrO$_3$ and BaZrO$_3$ Perovskites, *Phys. Chem. Miner.*, 1991, **18**(5), p 294-301 (in English)

11. X.Q. Cao, R. Vassen, F. Tietz, and D. Stöver, New Double-Ceramic-Layer Thermal Barrier Coatings Based on Zirconia–rare Earth Composite Oxides, *J. Eur. Ceram. Soc.*, 2006, **26**(3), p 247-251 (in English)

12. F. Tarasi, M. Medraj, A. Dolatabadi, R.S. Lima, and C. Moreau, Thermal Cycling of Suspension Plasma Sprayed Alumina-YSZ Coatings Containing Amorphous Phases, *J. Am. Ceram. Soc.*, 2012, **95**(8), p 2614-2621 (in English)

13. W. Ma, X.L. Jin, Y. Ren, S.P. Xing, Y. Bai, and H.Y. Dong, Synthesis and Thermophysical Properties of La$_2$Zr$_2$O$_7$/SrZrO$_3$ Composite as a New Thermal Barrier Coating Material, *Proceedings of the International Thermal Spray Conference 2015*, A. McDonald, A. Agarwal, G. Bolelli, A. Concustell, Y.-C. Lau, F.-L. Toma, E. Turenen, and C. Widener, Eds., May 11-14 2015 (Long Beach, CA), ASM International, 2015, p 867-872 (in English)

14. S. Krämer, J. Yang, and C.G. Levi, Infiltration-Inhibiting Reaction of Gadolinium Zirconate Thermal Barrier Coatings with CMAS Melts, *J. Am. Ceram. Soc.*, 2008, **91**(2), p 576-583 (in English)

15. L.H. Gao, H.B. Guo, S.K. Gong, and H.B. Xu, Plasma-sprayed La$_2$Ce$_2$O$_7$ Thermal Barrier Coatings Against Calcium-Magnesium-Alumina-Silicate Penetration, *J. Eur. Ceram. Soc.*, 2014, **34**(10), p 2553-2561 (in English)

16. H.B. Zhao, C.G. Levi, and H.N.G. Wadley, Molten Silicate Interactions with Thermal Barrier Coatings, *Surf. Coat. Technol.*, 2014, **251**, p 74-86 (in English)

17. U. Schulz and W. Braue, Degradation of La$_2$Zr$_2$O$_7$ and Other Novel EB-PVD Thermal Barrier Coatings by CMAS (CaO–MgO–Al$_2$O$_3$–SiO$_2$) and Volcanic Ash Deposits, *Surf. Coat. Technol.*, 2013, **235**, p 165-173 (in English)

18. B.J. Harder, J. Ramirez-Rico, J.D. Almer, K.N. Lee, and K.T. Faber, Chemical and Mechanical Consequences of Environmental Barrier Coating Exposure to Calcium–Magnesium–Aluminosilicate, *J. Am. Ceram. Soc.*, 2011, **94**(S1), p S178-S185 (in English)

19. X. Zhou, B.L. Zou, L.M. He, Z.H. Xu, J.Y. Xu, R.M. Mu, and X.Q. Cao, Hot Corrosion Behaviour of La$_2$(Zr$_{0.7}$Ce$_{0.3}$)$_2$O$_7$ Thermal Barrier Coating Ceramics Exposed to Molten Calcium Magnesium Aluminosilicate at Different Temperatures, *Corros. Sci.*, 2015, **100**, p 566-578 (in English)

20. K. Jiang, S. Liu, and C. Li, Nano-Nano Composite Powders of Lanthanum Zirconate and Yttria-Stabilized Zirconia by Spray Pyrolysis, *J. Am. Ceram. Soc.*, 2013, **96**(96), p 3296-3303 (in English)

21. D.L. Poerschke and C.G. Levi, Effects of Cation Substitution and Temperature on The Interaction Between Thermal Barrier Oxides and Molten CMAS, *J. Eur. Ceram. Soc.*, 2015, **35**(2), p 681-691 (in English)

22. J.M. Drexler, A.L. Ortiz, and N.P. Padture, Composition Effects of Thermal Barrier Coating Ceramics on Their Interaction with Molten Ca-Mg-Al-Silicate (CMAS) Glass, *Acta Mater.*, 2012, **60**(15), p 5437-5447 (in English)